

Scanning transmission electron microscopy (STEM) and analytical electron microscopy of biological and nano materials

R. D. Leapman¹, J. Zhang², J. S. Diamond², X. Chen³, T. S. Reese³, A. A. Sousa¹

1. Laboratory of Cellular Imaging & Macromolecular Biophysics, NIBIB, National Institutes of Health, Bethesda, MD 20892, USA

2. Synaptic Physiology Section, NINDS, National Institutes of Health, Bethesda, MD 20892, USA

3. Laboratory of Neurobiology, NINDS, National Institutes of Health, Bethesda, MD 20892, USA

leapmanr@mail.nih.gov

Keywords: STEM, analytical EM, electron tomography

The scanning transmission electron microscope (STEM) offers high collection efficiency for signals generated by interaction of a finely focused, nanometer-sized, electron probe, which makes STEM well suited for analyzing beam-sensitive biological specimens [1]. In particular, elastically scattered electrons collected by the STEM's annular dark-field detector (ADF) yield a signal that is proportional to the mass of a biological structure contained within the volume illuminated by the probe. This mass mapping technique enables molecular weights of large protein assemblies to be determined [2,3]. For example, it is possible to characterize the organization of subunits in filamentous proteins that have indefinite total mass but well defined mass-per-length, such as disease-associated amyloid fibrils [4,5]. The strong ADF elastic scattering signal from heavy atoms can also be applied to visualize heavy atom clusters, which are used to label specific protein assemblies in their cellular context [6].

By collecting the inelastic scattering signal using an electron energy loss spectrometer (EELS), it is possible to quantify the distributions of metal ions and low atomic number atoms contained within macromolecular complexes or subcellular compartments [7,8]. The STEM-EELS spectrum-imaging technique enables weak spectral features to be extracted, e.g., to measure minute concentrations of calcium, an important regulatory element, in specific subcellular compartments of freeze-dried preparations of cells and tissues [9]. It has also been possible to detect the iron cores of individual ferritin molecules distributed in regions of unstained brain, where iron regulates important cellular processes and, when stored as ferritin, gives rise to magnetic resonance imaging contrast [10].

A combination of STEM and EELS has been used in a number of laboratories to analyze the structure and composition of hybrid organic-inorganic bio-nanoparticles developed as diagnostic and therapeutic reagents in applications to nanomedicine [11-13].

Important advantages can be realized when the STEM is employed to perform electron tomography [14-20]. We have demonstrated that STEM tomography enables determination of the three-dimensional ultrastructure of embedded cells sectioned to a thickness of 1 to 2 μm [17-19]. Such specimens are considerably thicker than can be analyzed by conventional TEM tomography, for which resolution is limited by chromatic aberration of the objective lens due to multiply inelastic scattering. We have utilized a probe of small angular convergence (approximately 1 mrad) to give a diffraction-limited probe size of about 1 nm. The small angular convergence also results in a large depth-of-field throughout the specimen thickness since geometrical spreading of the probe is only a few nanometers. Moreover, the use of an on-axis bright-field detector reduces effects of beam broadening, since most electrons that undergo multiple elastic scattering in the lower part of thick specimens do not reach the detector (Fig. 1). Therefore, spatial resolution in bright-field STEM tomograms is improved relative to STEM tomograms acquired with an annular dark-field detector [17].

We have recorded dual-axis bright-field STEM tomograms in an FEI Tecnai TF30 transmission electron microscope equipped with a Shottky field emission gun operating at an acceleration voltage of 300 kV. Specimens were prepared by fixation, dehydration, embedding, ultramicrotomy and post-staining, with or without rapid freezing and freeze-substitution. Gold nanoparticles were deposited on the top and bottom surfaces of the sections to aid in alignment of the tilt series. Images were acquired over an angular range of $\pm 54^\circ$ after pre-irradiation with a broad beam in TEM mode to stabilize ultrastructure. Tomograms were reconstructed by means of the IMOD program (University of Colorado) [21], and were visualized with the Amira software package.

The STEM tomography approach is ideally suited to visualizing whole neuronal synapses, which have dimensions of order 0.5 to 1 μm , and for making quantitative measurements on the numbers, sizes and shapes of synaptic components. For example, we have applied the technique to study the architecture of two types of retinal ribbon synapses, which are specialized structures at presynaptic active zones encoding a wide dynamic range of sensory signals through continuous vesicle release. We have applied the technique to determine the full 3D architecture of ribbon synapses in mammalian (rat) cone photoreceptor cells and rod bipolar cells as shown in Fig. 2 [22,23].

In another application of STEM tomography, we have reconstructed entire spine postsynaptic densities (PSDs) in cortical regions of mouse brain. It was possible to determine the thickness, shape and area of PSDs for every synapse within defined $60 \mu\text{m}^3$ volumes of neuropil [24]. STEM tomography of thick sections provides a useful approach for determining the nanoscale structure of entire synapses in different types of neuronal tissues, which can help to gain insight into specialized synaptic function.

In summary, the STEM offers a variety of quantitative imaging modes for identifying heavy-atom labels, determining molecular mass, measuring elemental content, and elucidating the 3D structure of biological and bio-nanomaterials [25].

1. A.V. Crewe and J.S. Wall, *J. Mol. Biol.* 48 (1970) 375.
2. A. Engel, *Ultramicroscopy* 3 (1978) 273.
3. J.S. Wall and J.F. Hainfeld, *Ann. Rev. Biophys. Biophys. Chem.* 15 (1986) 355.
4. A.T. Petkova, et al., *Proc. Natl. Acad. Sci. USA* 99 (2002) 16742.
5. N. Norlin et al., *J. Struct. Biol.* 180 (2012) 174.
6. J.F. Hainfeld, *Science* 236 (1987) 450.
7. R.D. Leapman et al., *Ultramicroscopy* 49 (1993) 225.
8. R.D. Leapman, *J. Microsc.* 210 (2003) 5.
9. J. Feng, A.V. Somlyo and A.P. Somlyo, *J. Microsc.* 215 (2004) 92.
10. M. Fukunaga et al. *Proc. Natl. Acad. Sci. USA* 107 (2010) 3834.
11. M.M. van Schooneveld et al., *Nature Nanotech.* 5 (2010) 538.
12. R.D. Leapman, *Nature Nanotech.* 5 (2010) 480.
13. A.E. Porter et al., *Nature Nanotech.* 2 (2007) 713.
14. P.A. Midgley et al., *Ultramicroscopy* 96 (2003) 413.
15. I. Arslan, J.R. Tong and P.A. Midgley, *Ultramicroscopy* 106 (2006) 994.
16. A.E. Yakushevskaya et al., *J. Struct. Biol.* 159 (2007) 381.
17. M.F. Hohmann-Marriott et al., *Nature Methods* 6 (2009) 729.
18. A.A. Sousa et al., *Ultramicroscopy* 109 (2009) 213.
19. A.A. Sousa et al., *J. Struct. Biol.* 174 (2011) 107.
20. N. de Jonge and F.M. Ross, *Nature Nanotech* 6 (2011) 695.
21. J.R. Kremer, D.N. Mastrorarde and J.R. McIntosh, *J. Struct. Biol.* 116 (1996) 71.
22. J.S. Diamond, *Nature Neuroscience* 14 (2011) 1097.
23. J. Zhang et al., *Proc. ARVO* (2012) 4318.
24. X. Chen et al., *J Neurosci.* 31 (2011) 6329.
25. This research was supported by the intramural programs of NIBIB and NINDS, NIH.

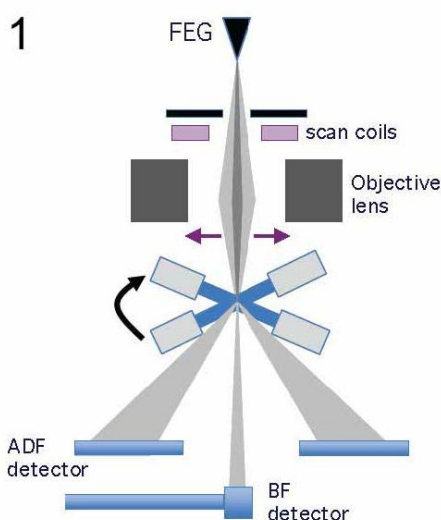


Figure 1. Schematic diagram of STEM tomography acquisition showing field-emission gun (FEG), scan coils, objective lens, and high-angle annular dark-field (ADF) and axial bright-field (BF) detectors.

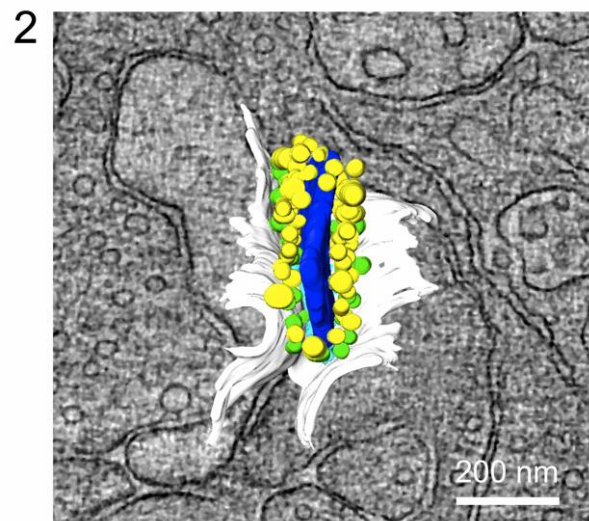


Figure 2. Ortho-slice through portion of dual-axis STEM bright-field tomogram of 1.2- μm thick section of stained rat retina, with superimposed visualization of entire ribbon synapse in cone photoreceptor cell. A central ribbon is evident with a series of docked vesicles (yellow); vesicles that are adjacent to the membrane are shown in green.